

## Quantum metric tensor of the Dicke model: Analytical and numerical study

Daniel Gutiérrez-Ruiz<sup>1,\*</sup>, Jorge Chávez-Carlos<sup>1,†</sup>, Diego Gonzalez<sup>1,2,‡</sup>, Jorge G. Hirsch<sup>1,§</sup> and J. David Vergara<sup>1,||</sup>

<sup>1</sup>*Instituto de Ciencias Nucleares, Universidad Nacional Autónoma de México, Apartado Postal 70-543, Ciudad de México 04510, Mexico*

<sup>2</sup>*Escuela Superior de Ingeniería Mecánica y Eléctrica - Instituto Politécnico Nacional (ESIME - IPN), 07738, CDMX, Mexico*



(Received 15 March 2022; revised 18 May 2022; accepted 24 May 2022; published 15 June 2022)

We compute both analytically and numerically the quantum metric tensor and its scalar curvature for the Dicke model. In the analytical setting we consider the thermodynamic limit and carry out the computations by means of the truncated Holstein-Primakoff approximation. We also study the exactly solvable case  $\omega_0 = 0$  and find that the corresponding non-Abelian QMT effectively reduces to just one metric tensor with zero determinant. In the numerical case we use an efficient basis to diagonalize the Hamiltonian for four different system's sizes. For the components of the quantum metric tensor and their derivatives, we find a remarkable agreement between the numerical and analytical results, with the metric's peaks signaling the precursors of the quantum phase transition. In the case of the scalar curvature, there are some differences between the numerical and analytical results that can be traced back to the behavior of the combination of the metric components' derivatives. Notably, the scalar curvature in the thermodynamic limit is continuous across the quantum phase transition and, in that zone, it approximately matches the numerical results.

DOI: [10.1103/PhysRevB.105.214106](https://doi.org/10.1103/PhysRevB.105.214106)

### I. INTRODUCTION

Studying the geometry of the quantum parameter space has given rise to exciting descriptions of various physical systems [1–5]. One of the preponderant elements in these studies is the quantum geometric tensor (QGT), which contains in its real part the quantum metric tensor (QMT) and in its imaginary part the Berry curvature. It is relevant for applications in quantum information processing, including adiabatic and holonomic quantum computing, where geodesics over the manifold of control parameters correspond to paths which minimize errors [6]. This tensor is essential in describing the quantum phase transitions (QPT) in the thermodynamic limit and gives much information about the precursors of these transitions if we consider systems with a finite number of particles. In the present work we study in detail the geometry of the quantum parameter space of the Dicke model. To our knowledge, the geometry of the quantum parameter space of the Dicke model has only been studied in the thermodynamic limit [7,8]. In this case, it is interesting that the Riemman curvature constructed from the QMT does not present a divergence in the QPT, and in the present article, we elaborate more on this point.

The Dicke model describes a system of  $\mathcal{N}$  two-level atoms collectively coupled with a quantized field, characterized by one bosonic mode. It provides a description of the superradiance phenomenon in light-matter systems [9–14]

and is useful to understand nonequilibrium dynamics [15–21] and in the study off the ultrastrong coupling regime in several systems [22–25]. In the thermodynamic limit its ground state exhibits a second order phase transition, has two classical degrees of freedom, and displays regular and chaotic dynamics, depending of the Hamiltonian parameters and the energy region analyzed [13,26–31]. Recently it was employed to analyze the relationship between classical chaos and the evolution of out-of-time-ordered correlators [32–34] and the presence of quantum scars [35,36].

The Dicke model has been realized in experiments with cavity assisted Raman transitions [37,38], trapped ions [39,40], and circuit quantum electrodynamics [41].

In this article we present a detailed study of the geometry of the quantum parameter space of the Dicke model, which has been previously studied only in the thermodynamic limit [7,8]. Analytical descriptions of the quantum metric tensor and its scalar curvature are obtained in the thermodynamic limit employing the truncated Holstein-Primakoff approximation, and also in the integrable limiting case  $\omega_0 = 0$ , which due to a degeneration of the system, has a non-Abelian QMT [42] with only one non-null metric tensor with zero determinant. These expressions are compared with extensive numerical results, performed employing an efficient basis, which allows the exact diagonalization of the Dicke Hamiltonian in a truncated basis, for different size systems, exploring wide parameter regions.

The most remarkable results are

- (i) There is a very good agreement between the numerical and analytical result for the components of the quantum metric tensor and their derivatives.
- (ii) The extreme points in the metric are clear precursors of the quantum phase transition, approaching the thermodynamic limits as the number of atoms is increased.

\*daniel.gutierrez@correo.nucleares.unam.mx

†jorge.chavez@ciencias.unam.mx

‡diego.gonzalez@correo.nucleares.unam.mx

§hirsch@nucleares.unam.mx

||vergara@nucleares.unam.mx

(iii) There are differences between the numerical and analytical results of the scalar curvature, associated with the combination of the derivatives of the metric components.

(iv) The scalar curvature in the thermodynamic limit is continuous across the quantum phase transition and, in that zone, it approximately matches the numerical results.

(v) The components of the Ricci tensor provide information about the behavior of the geodesics of the parameter space. Close to the phase transition, the area between two geodesics increases, implying that the quantum states are more separate for a slight variation of the parameters.

The paper is structured as follows. In Sec. II we provide a brief account of the basic elements to describe the parameter space geometry of a given quantum system. Then, Sec. III is devoted to the analytical computation of the QMT in the thermodynamic limit for both phases. In Sec. IV we present the analytical non-Abelian QMT of the case  $\omega_0 = 0$ . Section V describes the process of numerically computing the QMT and shows the analytical results along with their numerical counterparts close to resonance and far from it. After this, in Sec. VI we state our conclusions and suggest some future work. Finally, the Appendixes show some complementary computations and results.

## II. GEOMETRY OF THE PARAMETER SPACE

The fundamental object that endows the parameter space with a geometrical structure is the QGT, also known as the Fubini-Study metric. Given two quantum states  $|\psi(x)\rangle$  and  $|\psi(x + \delta x)\rangle$ , whose parameters  $x = \{x^i\}$  ( $i = 1, \dots, M$ ) differ infinitesimally, the components of the QGT are given by [1]

$$Q_{ij} = \langle \partial_i \psi | \partial_j \psi \rangle - \langle \partial_i \psi | \psi \rangle \langle \psi | \partial_j \psi \rangle, \quad (1)$$

where  $\partial_i := \frac{\partial}{\partial x^i}$ . The imaginary part of the QGT gives rise to the Berry curvature as

$$F_{ij} = -2\text{Im}Q_{ij}, \quad (2)$$

and its flux across an open surface in parameter space yields the celebrated Berry phase [43]. On the other hand, the real part of the QGT is the QMT, denoted as  $g_{ij}$ . This rank-two covariant tensor allows us to measure the distance between two quantum states infinitesimally apart, and has components given by

$$g_{ij} = \text{Re}Q_{ij}. \quad (3)$$

We observe that the quantum metric tensor is a direct generalization of the fidelity susceptibility when we take into account simultaneously several directions of the parameter space [4], and it measures the distance between quantum states for infinitesimal variations of the parameters, that is, how much a quantum state varies given a variation of the parameters. In particular, if we take  $|\psi(x)\rangle = |n(x)\rangle$ , where  $|n(x)\rangle$  is the eigenstate corresponding to a nondegenerate eigenvalue  $E_n(x)$  of the system's Hamiltonian  $\hat{H}(x)$ , then the adiabatic theorem guarantees that the system will remain in the  $n$ th state during evolution as long as the  $M$  parameters are slowly varying functions of time [44]. In this case, the QMT can be expressed

in a perturbative form as [2]

$$g_{ij}^{(n)} = \text{Re} \sum_{m \neq n} \frac{\langle n | \hat{O}_i | m \rangle \langle m | \hat{O}_j | n \rangle}{(E_m - E_n)^2}, \quad (4)$$

where the  $\hat{O}_i$ 's are the Hamiltonian deformations defined by

$$\hat{O}_i := \partial_i \hat{H}. \quad (5)$$

It is worth noting that in this nondegenerate case, the QGT (1) is invariant under the  $U(1)$  gauge transformation  $|n(x)\rangle \rightarrow e^{i\alpha_n(x)} |n(x)\rangle$ , where  $\alpha_n(x)$  is a smooth parameter-dependent function. Of course this property is also inherited by both the Berry curvature and the QMT.

Expression (4) stands out for the apparent singularities that would occur at level crossings, which are hallmarks of QPTs. In this sense, to determine whether or not the QMT has a genuine singularity, i.e., a singularity that cannot be removed by changing coordinates, we can use the scalar curvature  $R$ . This quantity is independent of the coordinates (parameters) and, for a two-dimensional manifold endowed with a metric tensor  $g_{ij}(x)$ , it can be found as

$$R = \frac{1}{\sqrt{|g|}} (\mathcal{A} + \mathcal{B}), \quad (6)$$

where  $g = \det[g_{ij}]$  and  $\mathcal{A}$  and  $\mathcal{B}$  are given by

$$\mathcal{A} := \partial_1 \left( \frac{g_{12}}{g_{11}\sqrt{|g|}} \partial_2 g_{11} - \frac{1}{\sqrt{|g|}} \partial_1 g_{22} \right), \quad (6a)$$

$$\mathcal{B} := \partial_2 \left( \frac{2}{\sqrt{|g|}} \partial_1 g_{12} - \frac{1}{\sqrt{|g|}} \partial_2 g_{11} - \frac{g_{12}}{g_{11}\sqrt{|g|}} \partial_1 g_{11} \right). \quad (6b)$$

In two dimensions, all components of the Riemann tensor can be written in the form

$$R_{ijkl} = (g_{ik}g_{jl} - g_{il}g_{jk}) \frac{R}{2}, \quad (7)$$

from this automatically follows the Ricci tensor

$$R_{ij} = g_{ij} \frac{R}{2}, \quad (8)$$

In this case, the Ricci tensor describes the change of an area element along the geodesics selected. In what follows, we study analytically and numerically the QMT, its scalar curvature, and the Ricci tensor for the Dicke model and discuss the information that these geometrical quantities are able to provide.

## III. QMT IN THE THERMODYNAMIC LIMIT

We begin this section with a succinct description of the main features of the Dicke model. The Dicke Hamiltonian is given by

$$\hat{H} = \omega_0 \hat{J}_z + \omega \hat{a}^\dagger \hat{a} + \frac{\gamma}{\sqrt{\mathcal{N}}} (\hat{a}^\dagger + \hat{a}) (\hat{J}_+ + \hat{J}_-), \quad (9)$$

where  $\omega_0$  is the excitation energy of the  $\mathcal{N}$  two-level atoms,  $\omega$  is the frequency of the single-mode radiation field described by the bosonic operators  $\hat{a}$  and  $\hat{a}^\dagger$ ,  $\gamma$  is the interaction parameter, and  $\hat{J}_z, \hat{J}_+, \hat{J}_-$  are the collective spin operators of the atomic part with pseudospin  $j = \mathcal{N}/2$ . Along this work we fix  $\hbar = 1$ .

The Dicke Hamiltonian (9) is invariant under the unitary transformation  $\hat{\Gamma} = e^{i\pi\hat{\Lambda}}$  with  $\hat{\Lambda} = \hat{a}^\dagger\hat{a} + \hat{J}_z + j$ . This symmetry allows the separation of the Hamiltonian matrix into two subspaces of definite parity [13,45], which is particularly useful for the numerical computations, as we show in Sec. V. We must notice that  $\mathbb{Z}_2$  symmetry induced by the parity transformation is a global symmetry, in contrast with the continuous symmetry that we will find in Sec. IV. An important feature of the Dicke model is the ground-state quantum phase transition that appears in the thermodynamic limit,  $j \rightarrow \infty$ , at the critical coupling  $\gamma_c = \sqrt{\omega\omega_0}/2$ , which separates the system into two phases: the normal phase and the superradiant phase. The normal phase exists for  $\gamma \leq \gamma_c$ , whereas the superradiant phase exists for  $\gamma > \gamma_c$ . The ground-state energy is given by

$$E_g = \begin{cases} -j\omega_0, & \gamma \leq \gamma_c, \\ -j\frac{\omega_0}{2}\left(\frac{\gamma_c^2}{\gamma^2} + \frac{\gamma^2}{\gamma_c^2}\right), & \gamma > \gamma_c. \end{cases} \quad (10)$$

We devote the next two subsections to the computation of the QMT of the ground state of the Dicke model in the thermodynamic limit  $j \rightarrow \infty$ . We fix  $\omega_0$  and take as our parameters  $x = \{x^i\} = (\gamma, \omega)$  with  $i = 1, 2$ .

### A. Normal phase

We begin the analysis with the normal phase ( $\gamma \leq \gamma_c$ ). The deformation operators associated with  $\gamma$  and  $\omega$  are

$$\hat{\mathcal{O}}_1 = \frac{\partial \hat{H}}{\partial \gamma} = \frac{1}{\sqrt{2j}}(\hat{a}^\dagger + \hat{a})(\hat{J}_+ + \hat{J}_-), \quad (11a)$$

$$\hat{\mathcal{O}}_2 = \frac{\partial \hat{H}}{\partial \omega} = \hat{a}^\dagger \hat{a}. \quad (11b)$$

We use the Holstein-Primakoff transformation [46], which is a way to associate bosonic operators to angular momentum operators, and is given by

$$\hat{J}_+ = \sqrt{2j} \hat{b}^\dagger \sqrt{1 - \frac{\hat{b}^\dagger \hat{b}}{2j}}, \quad (12a)$$

$$\hat{J}_- = \sqrt{2j} \sqrt{1 - \frac{\hat{b}^\dagger \hat{b}}{2j}} \hat{b}, \quad (12b)$$

$$\hat{J}_z = \hat{b}^\dagger \hat{b} - j. \quad (12c)$$

To consider the thermodynamic limit, we make the assumption that  $(\hat{b}^\dagger \hat{b})/2j \rightarrow 0$  when  $j \rightarrow \infty$ , thus expanding the square roots in Eq. (12) and truncating to zeroth order, which leads to

$$\hat{J}_+ \simeq \sqrt{2j} \hat{b}^\dagger, \quad \hat{J}_- \simeq \sqrt{2j} \hat{b}, \quad \hat{J}_z = \hat{b}^\dagger \hat{b} - j. \quad (13)$$

In this way the quadratic approximation of the Hamiltonian (9) turns out to be

$$\hat{H} \simeq -j\omega_0 + \omega_0 \hat{b}^\dagger \hat{b} + \omega \hat{a}^\dagger \hat{a} + \gamma(\hat{a}^\dagger + \hat{a})(\hat{b}^\dagger + \hat{b}), \quad (14)$$

and the approximated deformation operators (11) are

$$\hat{\mathcal{O}}_1 \simeq (\hat{a}^\dagger + \hat{a})(\hat{b}^\dagger + \hat{b}), \quad (15a)$$

$$\hat{\mathcal{O}}_2 = \hat{a}^\dagger \hat{a}. \quad (15b)$$

We clearly see from Eq. (14) that we are left with two coupled harmonic oscillators, so we need to diagonalize this Hamiltonian. To achieve this, we perform a Bogoliubov transformation to the operators  $\hat{c}_1$  and  $\hat{c}_2$  [see Eq. (A1)]. This process yields the diagonal Hamiltonian

$$\hat{H} \simeq -j\omega_0 + \omega_1 \hat{c}_1^\dagger \hat{c}_1 + \omega_2 \hat{c}_2^\dagger \hat{c}_2 + \frac{1}{2}(\omega_1 + \omega_2 - \omega - \omega_0), \quad (16)$$

with the frequencies  $\omega_1$  and  $\omega_2$  given by

$$\omega_1 = \sqrt{\frac{1}{2}\left(\omega^2 + \omega_0^2 - \sqrt{(\omega^2 - \omega_0^2)^2 + 16\gamma^2\omega\omega_0}\right)}, \quad (17a)$$

$$\omega_2 = \sqrt{\frac{1}{2}\left(\omega^2 + \omega_0^2 + \sqrt{(\omega^2 - \omega_0^2)^2 + 16\gamma^2\omega\omega_0}\right)}. \quad (17b)$$

Notice that at the QPT ( $\gamma = \gamma_c$ ) the frequency  $\omega_1$  vanishes. Furthermore, we can read off the ground-state energy looking at the dominant contribution in (16) when  $j \rightarrow \infty$ , which is  $E_g = -j\omega_0$  [cf. Eq. (10)].

With all these elements at hand, we can compute the QMT for the ground state via Eq. (4) as

$$g_{ij}^{(0)} = \text{Re} \sum_{n_1, n_2 \neq 0} \frac{\langle 0, 0 | \hat{\mathcal{O}}_i | n_1, n_2 \rangle \langle n_1, n_2 | \hat{\mathcal{O}}_j | 0, 0 \rangle}{(\omega_1 n_1 + \omega_2 n_2)^2}. \quad (18)$$

Once the QMT components are obtained, Eq. (6) can be used to compute the scalar curvature. We do not show the resulting expressions due to their length; instead, the plots of the QMT and  $R$  will be shown in Sec. V hand-in-hand with their numerical counterparts.

### B. Superradiant phase

We now analyze the superradiant phase. The relations  $\hat{J}_\pm = \hat{J}_x \pm i\hat{J}_y$  allow us to write the Hamiltonian (9) as

$$\hat{H} = \omega_0 \hat{J}_z + \omega \hat{a}^\dagger \hat{a} + \gamma \sqrt{\frac{2}{j}}(\hat{a}^\dagger + \hat{a})\hat{J}_x. \quad (19)$$

The first step to treat the superradiant phase is to displace the ground state. We can achieve this by rotating the angular momentum operators as

$$\begin{pmatrix} \hat{J}_x \\ \hat{J}_y \\ \hat{J}_z \end{pmatrix} = \begin{pmatrix} \cos \delta & 0 & \sin \delta \\ 0 & 1 & 0 \\ -\sin \delta & 0 & \cos \delta \end{pmatrix} \begin{pmatrix} \hat{J}'_x \\ \hat{J}'_y \\ \hat{J}'_z \end{pmatrix}, \quad (20)$$

and displacing the bosonic operators as

$$\hat{a} = \hat{a}' + \Delta, \quad \hat{a}^\dagger = \hat{a}'^\dagger + \Delta, \quad (21)$$

where  $\delta$  and  $\Delta$  have to be determined. To find the values of  $\delta$  and  $\Delta$ , we then use the truncated Holstein-Primakoff transformation but on the rotated operators  $\hat{J}'_x$  and  $\hat{J}'_z$ , i.e.,

$$\hat{J}'_x \simeq \sqrt{\frac{j}{2}}(\hat{b}'^\dagger + \hat{b}'), \quad \hat{J}'_z = \hat{b}'^\dagger \hat{b}' - j. \quad (22)$$

In this way we arrive at the Hamiltonian

$$\begin{aligned} \hat{H}' \simeq & \omega\Delta^2 + \omega\hat{a}'^\dagger\hat{a}' + \omega_0 \cos \delta (\hat{b}'^\dagger\hat{b}' - j) + \gamma \cos \delta (\hat{a}'^\dagger + \hat{a}')(\hat{b}'^\dagger + \hat{b}') + 2\sqrt{\frac{2}{j}}\gamma\Delta \sin \delta (\hat{b}'^\dagger\hat{b}' - j) \\ & + \sqrt{\frac{2}{j}}\gamma \sin \delta (\hat{a}'^\dagger + \hat{a}')\hat{b}'^\dagger\hat{b}' + (\hat{a}'^\dagger + \hat{a}')(\omega\Delta - \sqrt{2j}\gamma \sin \delta) + (\hat{b}'^\dagger + \hat{b}') \left( -\omega_0 \sin \delta \sqrt{\frac{j}{2}} + 2\gamma\Delta \cos \delta \right), \end{aligned} \quad (23)$$

which is valid for  $\gamma > \gamma_c$  and whose ground state corresponds to the superradiant phase.

We now require the vanishing of the terms in (23) that are linear in  $(\hat{a}'^\dagger + \hat{a}')$  and  $(\hat{b}'^\dagger + \hat{b}')$ , which leads to the two equations

$$\omega\Delta - \sqrt{2j}\gamma \sin \delta = 0, \quad (24a)$$

$$-\omega_0 \sin \delta \sqrt{\frac{j}{2}} + 2\gamma\Delta \cos \delta = 0. \quad (24b)$$

This allows us to solve for  $\delta$  and  $\Delta$ , obtaining

$$\Delta = \frac{\sqrt{2j(16\gamma^4 - \omega^2\omega_0^2)}}{4\omega\gamma}, \quad \cos \delta = \frac{\omega\omega_0}{4\gamma^2}. \quad (25)$$

Thus, plugging these values back into Eq. (23) and retaining only the quadratic terms in the creation and annihilation operators, we are left with

$$\begin{aligned} \hat{H}' \simeq & -j \left( \frac{2\gamma^2}{\omega} + \frac{\omega\omega_0^2}{8\gamma^2} \right) + \omega\hat{a}'^\dagger\hat{a}' + \frac{4\gamma^2}{\omega}\hat{b}'^\dagger\hat{b}' \\ & + \frac{\omega\omega_0}{4\gamma}(\hat{a}'^\dagger + \hat{a}')(\hat{b}'^\dagger + \hat{b}'). \end{aligned} \quad (26)$$

As in the normal phase, we now use a Bogoliubov transformation [see Eq. (A3)]. This results in the diagonal Hamiltonian for the superradiant phase

$$\hat{H}' \simeq -j \left( \frac{2\gamma^2}{\omega} + \frac{\omega_0^2\omega}{8\gamma^2} \right) + \omega'_1\hat{c}'_1{}^\dagger\hat{c}'_1 + \omega'_2\hat{c}'_2{}^\dagger\hat{c}'_2 - \frac{\omega}{2} - \frac{2\gamma^2}{\omega}, \quad (27)$$

with the frequencies  $\omega'_1$  and  $\omega'_2$  given by

$$\omega'_1 = \frac{1}{\omega} \sqrt{\frac{1}{2} \left( 16\gamma^4 + \omega^4 - \sqrt{(16\gamma^4 - \omega^4)^2 + 4\omega^6\omega_0^2} \right)}, \quad (28a)$$

$$\omega'_2 = \frac{1}{\omega} \sqrt{\frac{1}{2} \left( 16\gamma^4 + \omega^4 + \sqrt{(16\gamma^4 - \omega^4)^2 + 4\omega^6\omega_0^2} \right)}. \quad (28b)$$

The energy of the ground state in the superradiant phase is easily identified as the leading contribution in  $j$  in Eq. (27), which is [cf. Eq. (10)]

$$E_g = -j \left( \frac{2\gamma^2}{\omega} + \frac{\omega_0^2\omega}{8\gamma^2} \right). \quad (29)$$

We are ready to compute the QMT for the superradiant phase. We first read the approximated deformation operators

from the quadratic Hamiltonian (26), finding that

$$\hat{\mathcal{O}}'_1 \simeq \frac{8\gamma}{\omega}\hat{b}'^\dagger\hat{b}' - \frac{\omega\omega_0}{4\gamma^2}(\hat{a}'^\dagger + \hat{a}')(\hat{b}'^\dagger + \hat{b}'), \quad (30a)$$

$$\hat{\mathcal{O}}'_2 \simeq \hat{a}'^\dagger\hat{a}' - \frac{4\gamma^2}{\omega^2}\hat{b}'^\dagger\hat{b}' + \frac{\omega_0}{4\gamma}(\hat{a}'^\dagger + \hat{a}')(\hat{b}'^\dagger + \hat{b}'), \quad (30b)$$

where we have omitted the terms that do not contain creation or annihilation operators since they will not contribute to the QMT. All that remains is to substitute (30) into (18) using the frequencies (28). The corresponding plots of the QMT and  $R$  for this phase will be shown in Sec. V hand-in-hand with their numerical counterparts.

We close this section with a remark. As opposed to Refs. [7,8], we considered all the expressions in terms of the creation and annihilation operators without recourse to the quadratures  $\hat{q}$  and  $\hat{p}$ . This leads to QMT components that are similar to those of Refs. [7,8], but that have a different scalar curvature. At first, this may seem contradictory because it is well known that the scalar curvature is invariant under parameter transformations; however, the employed transformations combine both operators and parameters. In this sense, the most consistent approach is to take the original Hamiltonian to derive the deformation operators (5) that are required to compute the QMT.

#### IV. EXACTLY SOLVABLE CASE

Here we draw our attention to the case  $\omega_0 = 0$  for which the Hamiltonian (9) can be solved exactly. The resulting degenerate spectrum requires the utilization of the *non-Abelian* QMT [42,47]. We first provide a brief description of the non-Abelian QMT and then carry out its computation.

Consider a Hamiltonian whose  $n$ th state has degeneracy  $g_n$ , i.e.,

$$\hat{H}|n, I\rangle = E_n|n, I\rangle, \quad (31)$$

where  $I = 1, \dots, g_n$  distinguishes vectors from the same eigensubspace. The non-Abelian QMT for the  $n$ th state is given by [42,47]

$$Q_{ijIJ}^{(n)} = \langle \partial_i(n, I) | \partial_j(n, J) \rangle - \sum_{K=1}^{g_n} \langle \partial_i(n, I) | n, K \rangle \langle n, K | \partial_j(n, J) \rangle, \quad (32)$$

and the corresponding non-Abelian QMT is

$$g_{ijIJ}^{(n)} = \frac{1}{2} (Q_{ijIJ}^{(n)} + Q_{ijJI}^{(n)*}). \quad (33)$$

The corresponding non-Abelian Berry curvature, known as the Wilczek-Zee curvature [48], is given by  $F_{ijIJ}^{(n)} = i(Q_{ijIJ}^{(n)} -$

$Q_{ijIJ}^{(n)*}$ . Note that there are two types of indices: those corresponding to the parameter space  $(i, j, k, \dots)$ , and those corresponding to the  $n$ th degenerate subspace  $(I, J, K, \dots)$ . It is also worth noting that in this degenerate case, the QGT (32) is invariant under the  $SU(g_n)$  gauge transformation

$$|n, I\rangle \rightarrow \sum_{J=1}^{g_n} |n, J\rangle U_{JI}^{(n)}(x), \quad (34)$$

where  $U_{JI}^{(n)}(x)$  are the components of a  $g_n \times g_n$  parameter-dependent unitary matrix.

If we now differentiate (31) with respect to the parameters, it is not hard to arrive at the perturbative form of (32) given by

$$Q_{ijIJ}^{(n)} = \sum_{m \neq n} \sum_{K=1}^{g_n} \frac{\langle n, I | \hat{O}_i | m, K \rangle \langle m, K | \hat{O}_j | n, J \rangle}{(E_m - E_n)^2}, \quad (35)$$

where, just like in Eq. (5), the Hamiltonian deformations are  $\hat{O}_i = \partial_i \hat{H}$ .

We now return to the Dicke model and put  $\omega_0 = 0$  in (9), thus obtaining our Hamiltonian of interest which we call  $\hat{H}_0$ :

$$\hat{H}_0 = \omega \hat{a}^\dagger \hat{a} + \frac{2\gamma}{\sqrt{N}} (\hat{a}^\dagger + \hat{a}) \hat{J}_x. \quad (36)$$

To find the exact solution, we perform the operator transformation  $\hat{a} = \hat{A} - \frac{2\gamma}{\omega\sqrt{N}} \hat{J}_x$  and then the rotation  $\hat{J}_x = \hat{J}'_z$ ,  $\hat{J}_y = \hat{J}'_y$ ,  $\hat{J}_z = -\hat{J}'_x$  (see, for example, Ref. [49]), so that the Hamiltonian (36) becomes

$$\hat{H}_0 = \omega \hat{A}^\dagger \hat{A} - \frac{4\gamma^2}{\omega N} \hat{J}'_z{}^2. \quad (37)$$

The eigenstates of  $\hat{H}_0$  are formed as tensor products of boson states  $|N\rangle$  and angular momentum states  $|j, m'\rangle$ , and satisfy the equations

$$\hat{A}^\dagger \hat{A} |N; j, m'\rangle = N |N; j, m'\rangle, \quad (38a)$$

$$\hat{J}^2 |N; j, m'\rangle = j(j+1) |N; j, m'\rangle, \quad (38b)$$

$$\hat{J}'_z |N; j, m'\rangle = m' |N; j, m'\rangle, \quad (38c)$$

with  $j = N/2$ ,  $N = 0, 1, 2, \dots$  and  $m' = -j, \dots, j$ , which in turn implies that the spectrum is given by

$$E_{N;j,m'} = \omega N - \frac{2\gamma^2}{\omega j} m'^2. \quad (39)$$

It is easily seen from (39) that, for every  $N$ , the states with  $m'$  and  $-m'$  are degenerate, so the energy actually depends on the absolute value of  $m'$ ; we will make this explicit for our purposes, thus writing  $E_{N;j,|m'|}$ . Furthermore, we single out the degeneracy index, labeling every state as  $|N; j, |m'|, \pm\rangle$ , where  $\pm$  indicates the sign of  $m'$ . In particular, the ground states  $|0; j, j, \pm\rangle$  have the energy

$$E_{0;j,j} = -\frac{2\gamma^2}{\omega} j. \quad (40)$$

We are now ready to compute the non-Abelian quantum geometric tensor of the ground state which we denote as  $Q_{ijIJ}^{(0)}$ . Since the ground state is twofold degenerate, we will have four components in the uppercase subscripts that correspond to the possible combinations of the signs of  $m'$ :  $Q_{ij++}^{(0)}$ ,  $Q_{ij+-}^{(0)}$ ,  $Q_{ij--}^{(0)}$ , and  $Q_{ij--}^{(0)}$ . We begin by reading the deformation operators from the Hamiltonian (36) and then transforming them to act on the eigenstates  $|N; j, m'\rangle$ :

$$\hat{O}_1 = \frac{2}{\sqrt{N}} (\hat{a}^\dagger + \hat{a}) \hat{J}_x = \frac{2}{\sqrt{N}} \left( \hat{A}^\dagger + \hat{A} - \frac{4\gamma}{\omega\sqrt{N}} \hat{J}'_z \right) \hat{J}'_z, \quad (41a)$$

$$\hat{O}_2 = \hat{a}^\dagger \hat{a} = \hat{A}^\dagger \hat{A} - \frac{2\gamma}{\omega\sqrt{N}} (\hat{A}^\dagger + \hat{A}) \hat{J}'_z + \frac{4\gamma^2}{\omega^2 N} \hat{J}'_z{}^2. \quad (41b)$$

Specializing formula (35) to our case, the non-Abelian quantum geometric tensor reads as

$$Q_{ijIJ}^{(0)} = \sum_{N=0}^{\infty} \sum_{|m'|=0}^{\{j-1, j\}} \sum_{K=\{+, -\}} \frac{\langle 0; j, j, I | \hat{O}_i | N; j, |m'|, K \rangle \langle N; j, |m'|, K | \hat{O}_j | 0; j, j, J \rangle}{(E_{N;j,|m'|} - E_{0;j,j})^2}, \quad (42)$$

where  $\{j-1, j\}$  means that, to exclude the ground state, the sum in  $|m'|$  runs up to  $j-1$  for  $N=0$ , but up to  $j$  for  $N>0$ , and where  $I, J = \{+, -\}$  to form the four possible sign combinations. We have also assumed that  $j$  is an integer so that the sum in  $|m'|$  starts at zero. In the case that  $j$  is half-integer, the sum in  $|m'|$  would start at  $1/2$ .

We see that the only contribution to Eq. (42) comes from the expectation value of the operator  $\hat{\Gamma} := (\hat{A}^\dagger + \hat{A}) \hat{J}'_z$ , which is readily evaluated to give

$$\langle 0; j, j, I | \hat{\Gamma} | N; j, |m'|, \pm \rangle = \pm |m'| \sqrt{N} \delta_{0,N-1} \delta_{j,|m'|} \delta_{I,\pm}. \quad (43)$$

This greatly simplifies the computation of the non-Abelian quantum geometric tensor  $Q_{ijIJ}^{(0)}$ , which turns out to be real and symmetric and, due to Eq. (33), equal to the non-Abelian

QMT  $g_{ijIJ}^{(0)}$ . The result is

$$g_{ij++}^{(0)} = g_{ij--}^{(0)} = \frac{2j}{\omega^2} \begin{pmatrix} 1 & -\frac{\gamma}{\omega} \\ -\frac{\gamma}{\omega} & \frac{\gamma^2}{\omega^2} \end{pmatrix} \quad (44)$$

and

$$g_{ij+-}^{(0)} = g_{ij-+}^{(0)} = \begin{pmatrix} 0 & 0 \\ 0 & 0 \end{pmatrix}. \quad (45)$$

Therefore, the non-Abelian QMT effectively reduces to one matrix. It is worth noting that the determinant of Eq. (44) vanishes. This is easily understood because the elimination of the parameter  $\omega_0$  makes it possible to factor out  $\omega$  or  $\gamma$  in the Hamiltonian (36), thus leaving one effective parameter. This behavior has also been observed in a previous work [50].

## V. QMT FOR FINITE SIZES

In this section we first provide the required elements for the numerical computation of the QMT and its scalar curvature for finite  $j$ , and then we show the results and compare them with their analytical counterparts in two regions: close to resonance and far from it.

### A. Description of the method

In order to diagonalize the Dicke Hamiltonian, we use an efficient basis [49,51], which corresponds to the eigenstates of the Dicke models in the integrable limit  $\omega_0 \rightarrow 0$  described above. We write it as  $|N; j, m'\rangle$ , where  $m'$  are the eigenvalues of  $\hat{J}_x$  and  $N$  is the eigenvalue of the  $\hat{A}^\dagger \hat{A}$  operator, with  $\hat{A} = \hat{a} + \frac{2\gamma}{\omega\sqrt{N}}\hat{J}_x$ ,

$$|N; j, m'\rangle = \frac{1}{\sqrt{N!}}(\hat{A}^\dagger)^N |N=0; j, m'\rangle. \quad (46)$$

The vacuum for a given  $m'$  is a boson coherent state ( $|\alpha\rangle$ ) times an eigenstate of the  $\hat{J}_x$  operator:

$$|N=0; j, m'\rangle = \left| \alpha = -\frac{2\gamma m'}{\omega\sqrt{N}} \right\rangle |jm'\rangle. \quad (47)$$

Employing the parity properties of the state  $|N=0; j, m'\rangle$  discussed in Appendix B, the  $k$ th excited-state wave function of the Dicke Hamiltonian can be written as

$$|\Psi^k\rangle = \sum_{N=0}^{N_{\max}} \sum_{m'=0}^j C_{N,m'}^k |N; j, m'; p=+\rangle. \quad (48)$$

Here  $C_{N,m'}^k$  are the coefficients of the  $k$ th wave function in terms of the extended bosonic basis with parity well defined and  $N_{\max}$  is the value of the truncation or cutoff in the number of displaced excitations ( $0 \leq N \leq N_{\max}$ ).

We define the departure for exact precision in the calculated wave function as

$$\Delta P^k = \sum_{m'=0}^j |C_{N_{\max},m'}^k|^2. \quad (49)$$

For a given value of  $N_{\max}$ , the set of converged eigenstates includes the ground state, and all with higher excitation energies up to the first whose value of  $\Delta P^k$  is larger than certain tolerance (usually  $10^{-3}$ )  $N_{\max}$ .

Employing the efficient basis with well-defined parity, we calculate the elements of the metric tensor  $g_{ij}(x)$  for the ground state as follows:

$$g_{ij}^{(0)} = \sum_{k \neq 0} \frac{\langle \Psi^0 | \hat{O}_i | \Psi^k \rangle \langle \Psi^k | \hat{O}_j | \Psi^0 \rangle}{(E_k - E_0)^2}. \quad (50)$$

The cutoff  $N_{\max}$  is selected to guarantee that this expression, evaluated using the converged eigenstates  $|\Psi^k\rangle$ , has also converged. In what follows, analytical and numerical results for the QMT and the scalar curvature are presented in three regions. One is in resonance:  $\omega = \omega_0 = 1.0$ , the second is close to it, with  $\omega = 1.0$ ,  $\omega_0 = 0.8$ , in both cases with  $\gamma \in \{0.3, 2.0\}$ . The third region is close to the integrable limit  $\omega_0 = 0$ . We selected  $\omega_0 = 0.01$ , and studied the region  $\omega \in \{0.16, 0.20\}$  and  $\gamma \in \{0.01, 0.05\}$ .

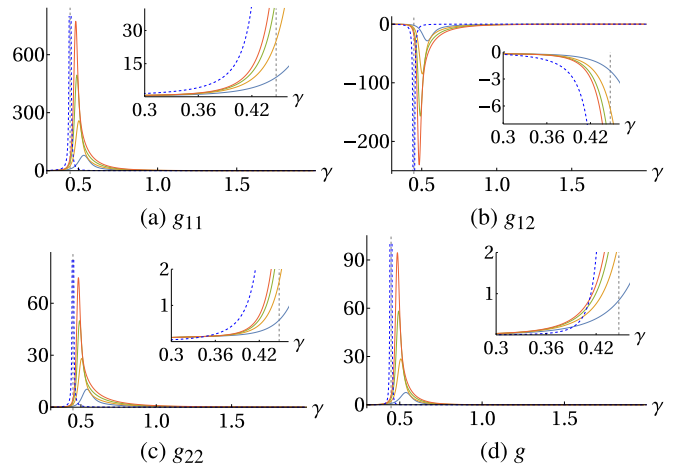


FIG. 1. QMT components and its determinant in the thermodynamic limit (dashed blue) and in the case  $j=5$  (solid blue),  $j=10$  (solid orange),  $j=15$  (solid green), and  $j=20$  (solid red) with  $\omega_0 = 1$  and  $\omega = 0.8$ . The critical value  $\gamma_c = 0.447$  is indicated by the vertical gray dashed line.

The numerical calculations presented are extremely demanding in terms of computational resources. The details are given in Appendix C. To obtain the derivatives of the QMT needed to calculate the scalar curvature, a large number of diagonalizations of the Hamiltonian must be performed for each value of  $j$ , varying  $\omega_0$  and  $\gamma$  in steps as small as 0.0002. Even for the calculations done along the line  $\omega_0 = 1.0$  (or 0.8), at least 16 values around the central one were needed to obtain the derivatives with respect to this parameter. For the third region, in the rectangle  $\gamma \in [0.01, 0.05]$  and  $\omega \in [0.16, 0.2]$  40 000 diagonalizations were performed for each value of  $j$ , with  $N_{\max} = 70$ .

### B. Results close to resonance

In Figs. 1 and 2 we compare the analytical QMT components and its determinant with their numerical counterparts for four different values of  $j$ . Having set  $\omega = 1$ , we study two regions around the value  $\omega_0 = 1$  and  $\omega = 0.8$ , varying  $\gamma$  in the range  $\{0.3, 2.0\}$ .

It can be observed in Fig. 1 there is a good agreement between the analytical and numerical results except near the critical region. However, in the numerical curves we clearly see that the peaks grow (positively for  $g_{11}$ ,  $g_{22}$ , and  $g$ , and negatively for  $g_{12}$ ) and get closer to the critical point  $\gamma_c$  as  $j$  increases, thus approaching the analytical curves. This indicates that the peaks signal the precursors of the QPT for finite  $j$  and implies that for  $j \rightarrow \infty$  those peaks will turn into singularities. The insets show a zoom over a small region to better display the good matching between the analytical and numerical curves. Similarly, Fig. 2 shows the QMT components and its determinant under resonance at  $\omega = \omega_0 = 1$ , whose behavior is analogous to that of the previous figure.

Figure 3 shows a three-dimensional plot of the analytical scalar curvature  $R$  for  $\omega_0 = 1$ , as a function of  $\omega$  and  $\gamma$ . The surface takes a furrowlike shape along the separatrix which is marked by the cyan line. We observe that  $R$  has a singularity at  $\gamma = 0$ , where it diverges positively. As we begin to

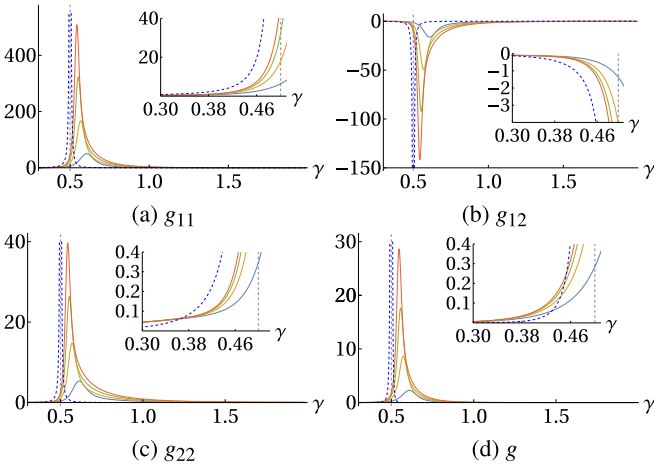


FIG. 2. QMT components and its determinant in the thermodynamic limit (dashed blue) and in the case  $j = 5$  (solid blue),  $j = 10$  (solid orange),  $j = 15$  (solid green), and  $j = 20$  (solid red) with  $\omega_0 = 1$  and  $\omega = 1$ . The critical value  $\gamma_c = 0.5$  is indicated by the vertical gray dashed line.

move away from  $\gamma = 0$ , the scalar curvature keeps descending until it reaches  $\gamma_c$  at the QPT, where it takes the value of  $-4$ . After this, the curve starts growing with a sharp slope, reaching a local maximum and then falling asymptotically to a constant value. It is worth noting that, despite the singularity that the QMT components and the determinant show at the critical coupling  $\gamma_c$ , the scalar curvature is continuous there, although not smooth. This means, as stated in Sec. II, that the singularity in the metric components and the determinant is removable. We also observe that the local maximum to the right of the separatrix decreases as  $\omega$  approaches zero, and it completely flattens out at  $\omega = 0$ .

In Fig. 4 we compare the analytical and numerical scalar curvatures. However, the curves are similar near the critical region. One piece of information that the curvature scalar gives us exclusively is whether the singularity associated with the phase transition is a singularity independent of the coordinate system, in this case of the selected parameters, or depends on

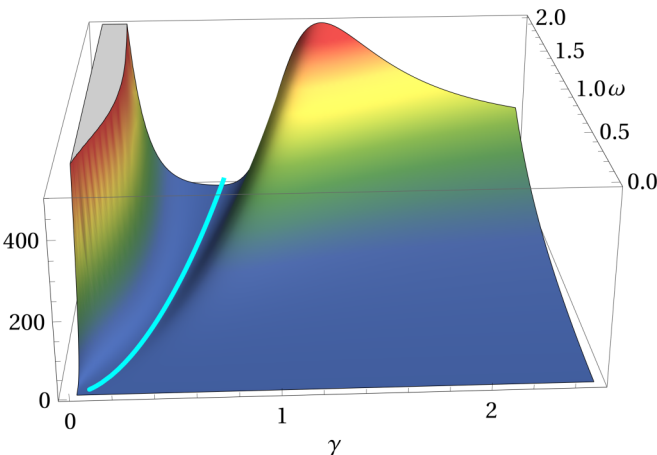


FIG. 3. Scalar curvature  $R$  of the QMT in the thermodynamic limit with  $\omega_0 = 1$ . The cyan line indicates the separatrix of the QPT.

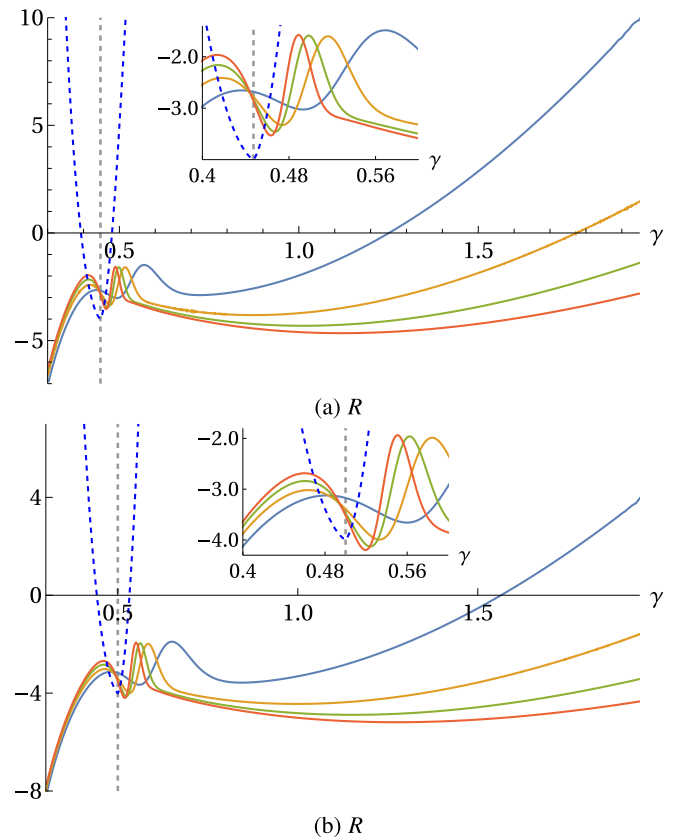


FIG. 4. Scalar curvature  $R$  of the QMT in the thermodynamic limit and in the case  $j = 5$  (solid blue),  $j = 10$  (solid orange),  $j = 15$  (solid green), and  $j = 20$  (solid red) with  $\omega_0 = 1$ . The case  $\omega = 0.8$  is shown in (a) and the case  $\omega = 1$  is shown in (b). The insets show a zoom over the critical region.

the selected parameters. In our case, we observe from Fig. 4 that both the analytical and numerical results tell us that the curvature scalar does not suffer a discontinuity or a divergence in the phase transition, which clearly shows that this quantum phase transition is dependent on the parameters. Furthermore, we note that the behavior of the analytical and numerical is strikingly different before and after the QPT. Note that the analytical scalar curvature diverges positively at  $\gamma = 0$ , whereas the numerical  $R$  falls to  $-\infty$  at that same point. Moreover, for  $\gamma > \gamma_c$ , the analytical curve sharply ascends, while the numerical one has a small local maximum and a local minimum, and then it slowly goes up. It can be noticed that as  $j$  increases, the slope of the scalar curvature decreases, although we cannot infer the behavior for bigger values of  $\gamma$  since the study of that region requires increased numerical efforts.

To understand the discrepancy between the analytical and numerical curves of the scalar curvature, we draw our attention to the derivatives of the QMT components and its determinant, which are the required functions to compute  $R$  [see Eqs. (6a) and (6b)]. All the first and second derivatives are shown in Fig. 17 in Appendix D, where we see that, just like with the QMT components, there is a remarkable agreement between the analytical and numerical derivatives. While both the analytical and numerical curves of the QMT components

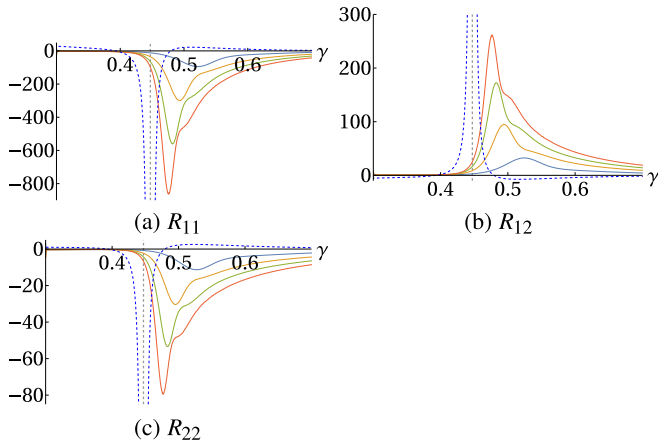


FIG. 5. Components of the Ricci tensor in the thermodynamic limit (dashed blue) and in the case  $j = 5$  (solid blue),  $j = 10$  (solid orange),  $j = 15$  (solid green), and  $j = 20$  (solid red) with  $\omega_0 = 1$  and  $\omega = 0.8$ . The critical value  $\gamma_c = 0.447$  is indicated by the vertical gray dashed line.

and their derivatives vary smoothly with  $\gamma$  and  $\omega$ , the scalar curvature has a high sensitivity of the combination of the QMT components' derivatives in Eqs. (6a) and (6b), causing the strong deviation between the analytical and numerical results far from the phase transition.

An additional ingredient that we study is to consider the components of the Ricci tensor that tell us in the directions defined by the unit vectors of the parameter space  $\hat{x}_1 = \hat{\gamma}$ ,  $\hat{x}_2 = \hat{\omega}$ , if the geodesics of the space of parameters repel or attract each other in the considered directions, depending on whether the Ricci tensor is negative or positive, respectively. Thus, we see from Figs. 5(a), 5(c), 6(a), 6(c), 7(a), and 7(c) that the negative Ricci tensor causes the geodesics to repel each other in that direction, which is equivalent to the metric components growing in these directions as the distances between the quantum states become larger and larger, and an area moving in these directions grows. Furthermore, in the analytical case,

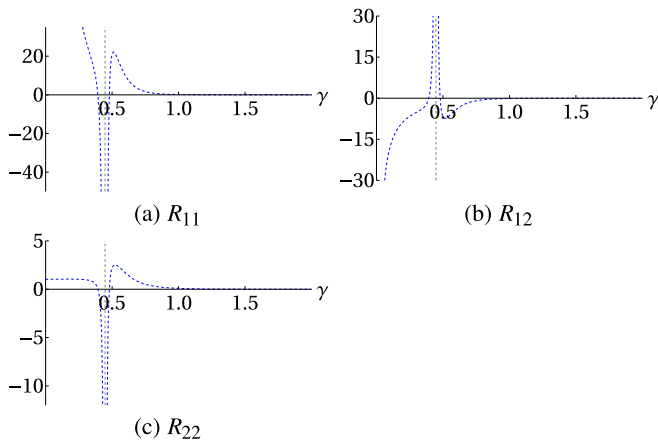


FIG. 6. Components of the Ricci tensor in the thermodynamic limit (dashed blue) with  $\omega_0 = 1$  and  $\omega = 0.8$ . The critical value  $\gamma_c = 0.447$  is indicated by the vertical gray dashed line. In the case  $\gamma \rightarrow 0$ , the component  $R_{22}$  takes the value 1.0307.

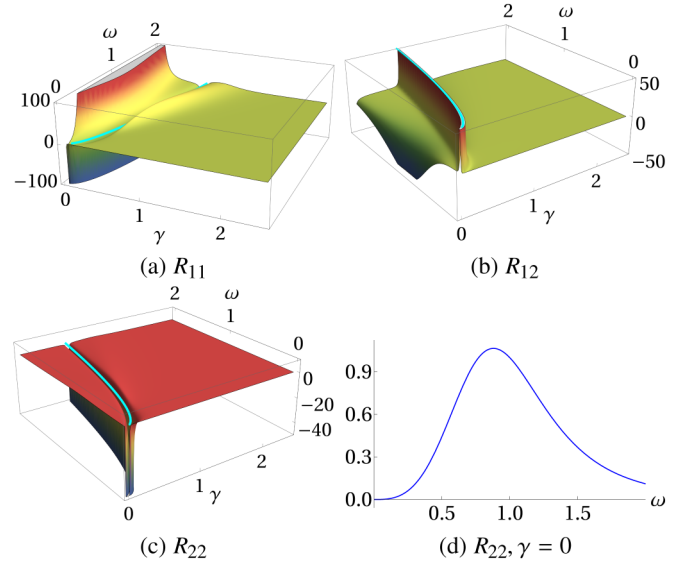


FIG. 7. Components of the Ricci tensor of the QMT in the thermodynamic limit with  $\omega_0 = 1$ . The cyan line indicates the separatrix of the QPT.

the transition is not traversable by the geodesics, while in the numerical case, since the Ricci tensor only reaches a finite value, the geodesics can cross it, and in this sense, we can only say that the minimum only marks the precursor of the phase transition. In addition, we observe from Figs. 5(b), 6(b) and 7(c) that in the case of the nondiagonal direction, the Ricci tensor is positive, which implies that the geodesics attract in this direction.

### C. Results far from resonance

The third region mentioned above is close to the integrable limit  $\omega_0 = 0$ , having  $\omega_0 = 0.01$ ,  $\omega \in \{0.16, 0.20\}$ , and  $\gamma \in \{0.01, 0.05\}$ .

The components of the QMT and its determinant in the thermodynamic limit are presented in Figs. 8(a), 8(c), 8(d), and 8(g). They show a clear divergence along the phase transition, and nearly no structure far from it.

The scalar curvature in the thermodynamic limit is shown in Fig. 9. Its behavior is similar as in the previous regions: it diverges at  $\gamma \rightarrow 0$ , decreases approaching the phase transition line, shown in cyan, reaches its minimum, grows again to attain a local maximum, and slowly decreases as  $\gamma$  keeps growing. In Fig. 10, it is shown that the scalar curvature is negative near the phase transition.

The components of the QMT and its determinant, obtained numerically for  $j = 20$ , are displayed in Figs. 8(b), 8(d), 8(f), and 8(h). As in the previous regions, their qualitative behavior is similar to the analytical analysis, exhibiting the precursors of the phase transitions as local maxima (minimum for  $g_{12}$ ), for values of  $\gamma$  slightly larger the cyan line, which depicts the thermodynamic limit.

In Fig. 11 those maxima are plotted in the  $\omega$ - $\gamma$  plane as colored dots, and their averages as black lines, and compared with the separatrix in the thermodynamic limit, shown in magenta. It is clear that they follow the same directions, but

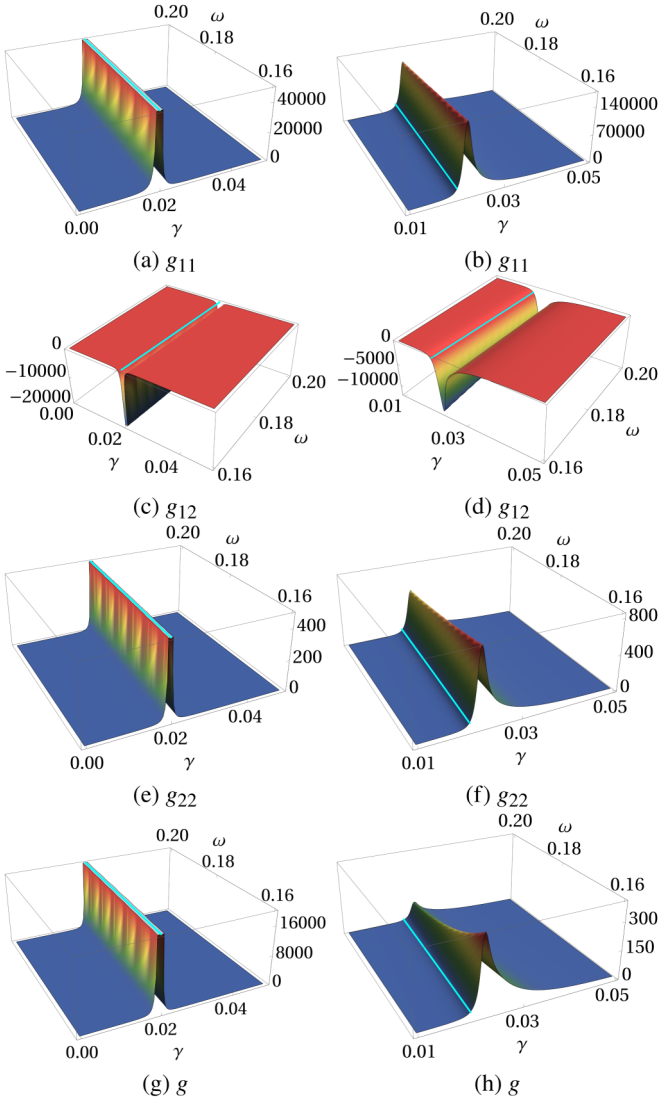


FIG. 8. Components of the QMT and its determinant in the thermodynamic limit [(a), (c), (e), and (g)] and in the case  $j = 20$  [(b), (d), (f), and (h)] with  $\omega_0 = 0.01$ . The cyan line is the separatrix.

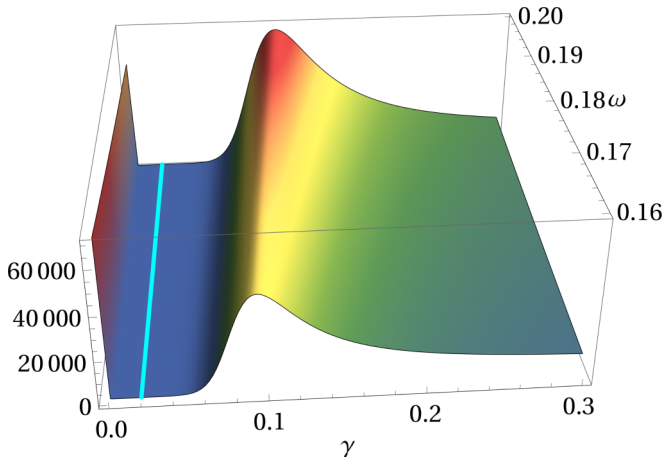


FIG. 9. Scalar curvature  $R$  of the QMT in the thermodynamic limit with  $\omega_0 = 0.01$ . The cyan line is the separatrix.

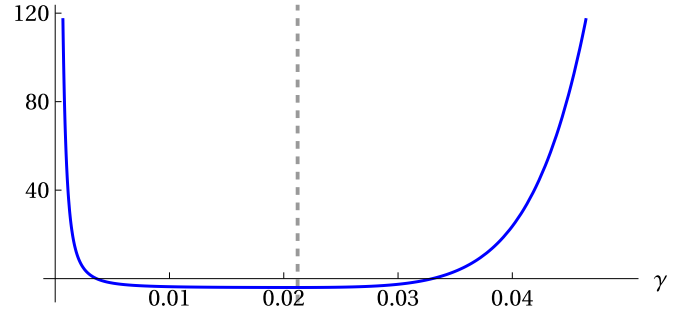


FIG. 10. Scalar curvature  $R$  of the QMT in the thermodynamic limit for  $\omega = 0.18$  and  $\omega_0 = 0.01$ . The critical value  $\gamma_c = 0.0212$  is indicated by the vertical gray dashed line.

the numerical results run along larger values of  $\gamma$  than the separatrix. The stepped structure of the dots corresponds to the step 0.0002 employed to vary  $\gamma$  in the calculations.

As in this region we selected  $\omega_0 = 0.01$ , the expression for the separatrix is  $\gamma_c = \sqrt{\omega\omega_0}/2 = 0.05\omega^{0.5}$ . The functions fitting the points of Fig. 11 are

$$\gamma = 0.0555\omega^{0.4997} \quad \text{for } g_{11}^{\max}, \quad (51)$$

$$\gamma = 0.0557\omega^{0.5006} \quad \text{for } g_{12}^{\max}, \quad (52)$$

$$\gamma = 0.0557\omega^{0.4994} \quad \text{for } g_{22}^{\max}, \quad (53)$$

$$\gamma = 0.0570\omega^{0.5019} \quad \text{for } g^{\max}, \quad (54)$$

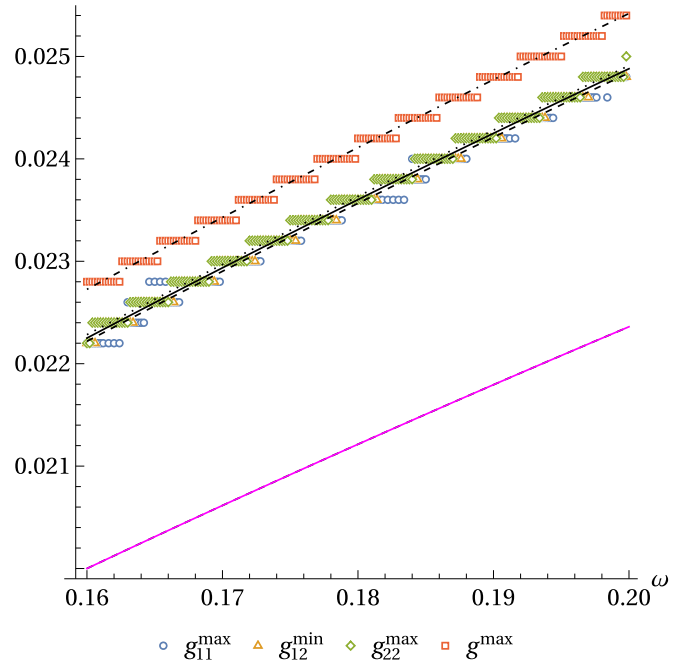


FIG. 11.  $\gamma_c$  and  $\gamma$  for the maximum of QMT components and its determinant in the case  $j = 20$  with  $\omega_0 = 0.01$ . The plot also shows the separatrix (solid magenta line) and the fit of Eqs. (51), (52), (53), and (54) for  $g_{11}^{\max}$  (dashed black line),  $g_{12}^{\min}$  (solid black line),  $g_{22}^{\max}$  (dotted black line), and  $g^{\max}$  (dot-dashed black line), respectively.

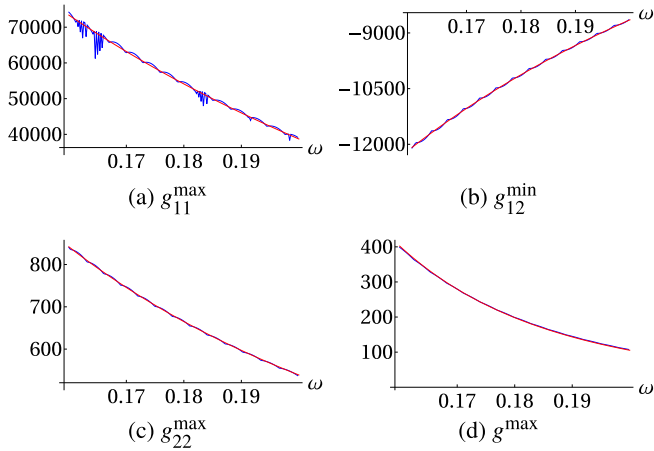


FIG. 12. Maximum of QMT components and its determinant in the case  $j = 20$  with  $\omega_0 = 0.01$ .

which confirm that the numerical and analytical curves are parallel, with the same exponent very close to  $1/2$ .

The fact that the numerical calculations of the components of the QMT and its determinant exhibit a finite maxima, instead of the divergent behavior, along the phase transition, allows us to determine the value of these maxima as functions of  $\omega$ . Their numerical values are displayed in blue in Fig. 12, showing small numerical fluctuations, and the red curves are smoothed fits, whose explicit expressions are presented in Eqs. (55), (56), (57), and (58):

$$g_{11}^{\max} = \frac{27741.6}{\omega}, \quad (55)$$

$$g_{12}^{\min} = -\frac{773.4}{\omega^{3/2}}, \quad (56)$$

$$g_{22}^{\max} = \frac{21.55}{\omega^2}, \quad (57)$$

$$g^{\max} = \frac{0.0067}{\omega^6}. \quad (58)$$

These are quite interesting results, which can be compared with the analytical ones obtained in the integrable limit  $\omega_0 =$

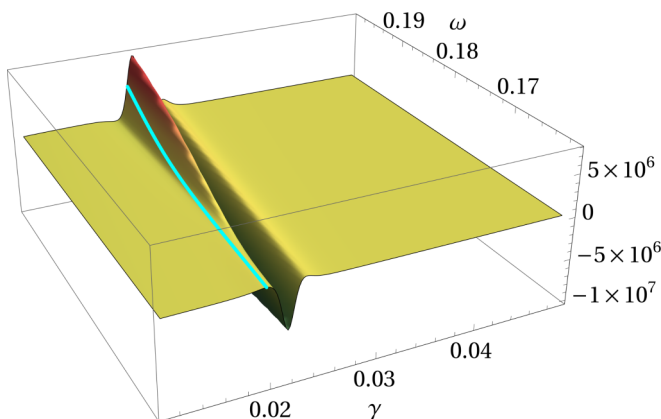


FIG. 13. Scalar curvature  $R$  of the QMT in the case  $j = 20$  with  $\omega_0 = 0.01$ . The cyan line is the separatrix.

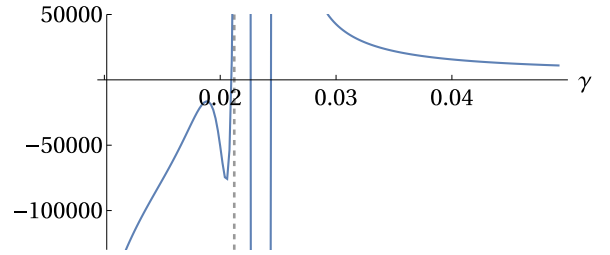


FIG. 14. Scalar curvature  $R$  of the QMT in the case  $j = 20$  with  $\omega = 0.18$  and  $\omega_0 = 0.01$ . The critical value  $\gamma_c = 0.0212$  is indicated by the vertical gray dashed line.

0. In this case, the components of the QMT, shown in Eq. (44), decay as  $\omega^{-2}$ ,  $\omega^{-3}$ , and  $\omega^{-4}$  for  $g_{11}$ ,  $g_{12}$ , and  $g_{22}$ , respectively, for the cases  $++$  and  $--$ , and are null for the cases  $+-$  and  $-+$ . Our fit shows that, when the exact symmetry is broken, with  $\omega_0$  very small but not zero, the exponents of  $\omega$  of the components of the QMT have the average values of these extreme cases.

The determinant is also interesting. Its values are far smaller of those of the individual components of the QMT, anticipating its null value at the exact limit. It goes as  $\omega^{-6}$ , which would be the behavior of the analytical expression, if it were non null, as it is.

The scalar curvature in this region is presented in Fig. 13. It acquires finite but very large positive and negative values close to the phase transition. A cut at  $\omega = 0.18$  is shown in Fig. 14 to exhibit that the scalar curvature diverges to negative values as  $\gamma \rightarrow 0$ , at variance with the analytical results, which diverge in the positive direction. We should note here that in the limit  $\gamma \rightarrow 0$ , the Hamiltonian for the analytical results (14) goes to two decoupled oscillators while in the limit  $\gamma \rightarrow 0$  the Hamiltonian (9) used for the numerical results goes to a harmonic oscillator and a rigid rotor and is quite remarkable that scalar curvature uncovers this difference. For large values of  $\gamma$  the scalar curvature decreases slowly to positive values.

As in the other regions, the behavior of the numerical results for the components of the QMT and its determinant, as functions of  $\gamma$  and  $\omega$ , resemble closely the analytical ones, obtained in the thermodynamic limit, and be understood as their precursors. The scalar curvature, on the other hand, only has similitudes close to the phase transitions. Additional analysis are needed to fully understand their differences. Figure 15 shows the components of the Ricci tensor, comparing the numerical and the analytical results in the thermodynamic limit for  $j = 20$ .

## VI. CONCLUSIONS

In this paper we have computed the QMT and its scalar curvature for the Dicke model using analytical and numerical techniques. On the analytical side we considered the thermodynamic limit and employed the truncated Holstein-Primakoff approximation to yield quadratic Hamiltonians for the normal and superradiant phases. On the numerical side we fixed the values of  $j$  and  $\omega_0$  and defined a grid in parameter space that allowed us to diagonalize the Hamiltonian matrix at every point using the efficient coherent basis. We showed that there is a good agreement between the analytical and numerical

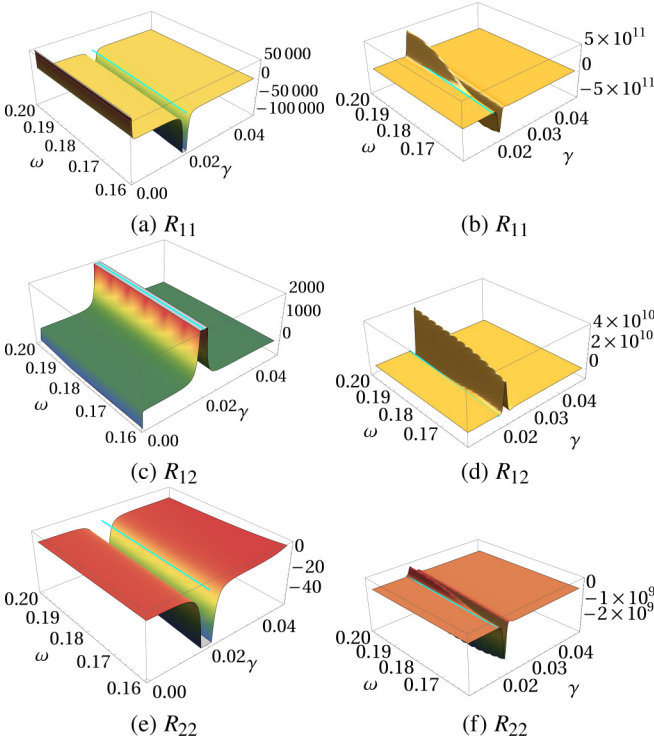


FIG. 15. Components of the Ricci tensor in the thermodynamic limit [(a), (c), and (e)] and in the case  $j = 20$  [(b), (d), and (f)] with  $\omega_0 = 0.01$ . The cyan line is the separatrix.

QMT components even for small values of  $j$ , and that the behavior of the peaks signal the singularities that will appear in the thermodynamic limit. Furthermore, we also compared the analytical and numerical scalar curvatures, observing close concordance near the QPT, but important discrepancies away from it. By studying the derivatives of the QMT components, we concluded that the differences are due to the combination of the various terms that appear in Eqs. (6a) and (6b).

The integrable case  $\omega_0 = 0$  was also studied analytically, and compared with numerical results for  $\omega_0 = 0.01$ . It was shown that the maxima of the components of the QMT have a functional dependence on  $\omega$  which is closely related to the exact case, and the numerical determinant is far smaller than any of the components, anticipating its null analytical value.

We would like to make two fundamental observations drawn from our results. First, the analytical computation of the QMT made use of the quadratic Hamiltonians that correspond to every phase in terms of the original creation and annihilation operators. As was discussed in Sec. III, we did not use a parameter-dependent operator transformation to arrive at our effective Hamiltonians since that would alter the value of the QMT and its scalar curvature; this was validated by the numerical results. Furthermore, it is remarkable that the curvature scalar is quite sensitive to the difference in the limits of  $\gamma \rightarrow 0$  of our two analytical and the numerical results, showing that this quantity is worth analyzing independently of the quantum metric tensor components.

It must be mentioned that in a previous work concerning the Lipkin-Meshkov-Glick model [52], we also observed a difference in the analytical and numerical scalars near the point of zero coupling. And second, the numerical results

that we obtained provide the only known QMT and scalar curvature for finite  $j$  and constitute one of the most valuable results of this paper. Remarkably, the numerical results also show that the peaks in all the metric components and the scalar curvature are signs of the QPT precursor, and they even appear for relatively small values of  $j$ . Naturally the exigence on computing resources grows as  $j$  increases, which makes it difficult to study the higher system's sizes for the moment.

The implementation of numerical techniques allows an extension of this work to study the ESQPT in the Dicke model and find out if there is a special behavior of the QMT and the scalar curvature in the known chaotic regions of the phase space [28,31,53]. Along these lines we could also use a chaos indicator like the Frobenius norm of the adiabatic gauge potential [54], which can be written in terms of a sum of elements of the QMT. Moreover, with the QMT at hand, it would be worth studying the Fubini-Study and Nielsen complexities which are of importance in the context of information theory and quantum computing [55,56]. Of course we could also explore other geometrical aspects like geodesics and their relation to QPTs [3].

## ACKNOWLEDGMENTS

We acknowledge the support of the Computing Center-ICN, in particular, of E. Palacios, L. Díaz, and E. Murrieta. We thank J. L. Gómez-Muñoz and F. Delgado who designed the Quantum add-on for Mathematica [57] that was used in the analytical computations. J.C.-C. was supported by a DGAPA-UNAM postdoctoral fellowship. D.G.-R. was partially supported by CONACyT Ph.D. Scholarship No. 332577. This work was partially supported by DGAPA-PAPIIT Grants No. IN105422 and No. IN104020.

## APPENDIX A: BOGOLIUBOV TRANSFORMATIONS

### 1. Normal phase

The Bogoliubov transformation that diagonalizes Hamiltonian (14) is

$$\hat{a} = \frac{\cos \alpha}{2\sqrt{\omega\omega_1}} [(\omega - \omega_1)\hat{c}_1^\dagger + (\omega + \omega_1)\hat{c}_1] + \frac{\sin \alpha}{2\sqrt{\omega\omega_2}} [(\omega - \omega_2)\hat{c}_2^\dagger + (\omega + \omega_2)\hat{c}_2], \quad (\text{A1a})$$

$$\hat{a}^\dagger = \frac{\cos \alpha}{2\sqrt{\omega\omega_1}} [(\omega - \omega_1)\hat{c}_1 + (\omega + \omega_1)\hat{c}_1^\dagger] + \frac{\sin \alpha}{2\sqrt{\omega\omega_2}} [(\omega - \omega_2)\hat{c}_2 + (\omega + \omega_2)\hat{c}_2^\dagger], \quad (\text{A1b})$$

$$\hat{b} = \frac{-\sin \alpha}{2\sqrt{\omega_0\omega_1}} [(\omega_0 - \omega_1)\hat{c}_1^\dagger + (\omega_0 + \omega_1)\hat{c}_1] + \frac{\cos \alpha}{2\sqrt{\omega_0\omega_2}} [(\omega_0 - \omega_2)\hat{c}_2^\dagger + (\omega_0 + \omega_2)\hat{c}_2], \quad (\text{A1c})$$

$$\hat{b}^\dagger = \frac{-\sin \alpha}{2\sqrt{\omega_0\omega_1}} [(\omega_0 - \omega_1)\hat{c}_1 + (\omega_0 + \omega_1)\hat{c}_1^\dagger] + \frac{\cos \alpha}{2\sqrt{\omega_0\omega_2}} [(\omega_0 - \omega_2)\hat{c}_2 + (\omega_0 + \omega_2)\hat{c}_2^\dagger], \quad (\text{A1d})$$

where  $\alpha$  is such that

$$\tan 2\alpha = \frac{4\gamma\sqrt{\omega\omega_0}}{\omega_0^2 - \omega^2}. \quad (\text{A2})$$

## 2. Superradiant phase

The Bogoliubov transformation that diagonalizes Hamiltonian (26) is

$$\begin{aligned} \hat{a}' &= \frac{\cos \alpha'}{2\sqrt{\omega\omega_1}} [(\omega - \omega_1')\hat{c}_1^{\dagger'} + (\omega + \omega_1')\hat{c}_1'] \\ &+ \frac{\sin \alpha'}{2\sqrt{\omega\omega_2}} [(\omega - \omega_2')\hat{c}_2^{\dagger'} + (\omega + \omega_2')\hat{c}_2'], \end{aligned} \quad (\text{A3a})$$

$$\begin{aligned} \hat{a}'^{\dagger} &= \frac{\cos \alpha'}{2\sqrt{\omega\omega_1}} [(\omega - \omega_1')\hat{c}_1' + (\omega + \omega_1')\hat{c}_1^{\dagger'}] \\ &+ \frac{\sin \alpha'}{2\sqrt{\omega\omega_2}} [(\omega - \omega_2')\hat{c}_2' + (\omega + \omega_2')\hat{c}_2^{\dagger'}], \end{aligned} \quad (\text{A3b})$$

$$\begin{aligned} \hat{b}' &= \frac{-\sin \alpha'}{4\gamma\sqrt{\omega\omega_1}} [(4\gamma^2 - \omega\omega_1')\hat{c}_1^{\dagger'} + (4\gamma^2 + \omega\omega_1')\hat{c}_1'] \\ &+ \frac{\cos \alpha'}{4\gamma\sqrt{\omega\omega_2}} [(4\gamma^2 - \omega\omega_2')\hat{c}_2^{\dagger'} + (4\gamma^2 + \omega\omega_2')\hat{c}_2'], \end{aligned} \quad (\text{A3c})$$

$$\begin{aligned} \hat{b}'^{\dagger} &= \frac{-\sin \alpha'}{4\gamma\sqrt{\omega\omega_1}} [(4\gamma^2 - \omega\omega_1')\hat{c}_1' + (4\gamma^2 + \omega\omega_1')\hat{c}_1^{\dagger'}] \\ &+ \frac{\cos \alpha'}{4\gamma\sqrt{\omega\omega_2}} [(4\gamma^2 - \omega\omega_2')\hat{c}_2' + (4\gamma^2 + \omega\omega_2')\hat{c}_2^{\dagger'}], \end{aligned} \quad (\text{A3d})$$

where  $\alpha'$  is such that

$$\tan 2\alpha' = \frac{2\omega^3\omega_0}{16\gamma^4 - \omega^4}. \quad (\text{A4})$$

## APPENDIX B: BASIS WITH DEFINED PARITY

The extended bosonic basis we used in this work to diagonalize the Dicke Hamiltonian is given by the eigenstates of the effective basis, which are (46). The previous states are not eigenvalues of the parity operator  $\hat{\Pi} = e^{i\pi\hat{\Lambda}} = e^{i\pi(\hat{J}_z+j)} e^{i\pi\hat{a}^{\dagger}\hat{a}}$ . In order to analyze the statistical properties of the Dicke spectrum, we have to separate the energy eigenstates according to their parity ( $p = \pm$ ). To this end, we construct a basis which is also an eigenbasis of the parity operator. It is easy to prove that

$$|N; j, m'\rangle = \frac{1}{\sqrt{N!}} \left( \hat{a}^{\dagger} + \frac{2\gamma}{\omega\sqrt{N}} m' \right)^N \Big|_{\alpha = -\frac{2\gamma m'}{\omega\sqrt{N}}} |jm'\rangle. \quad (\text{B1})$$

This result shows that states (46) are proportional to  $|jm'\rangle$ . It can be shown that the action of the rotation operator  $e^{i\pi(\hat{J}_z+j)}$  over  $|jm'\rangle$  gives

$$e^{i\pi(\hat{J}_z+j)} |jm'\rangle = |j - m'\rangle. \quad (\text{B2})$$

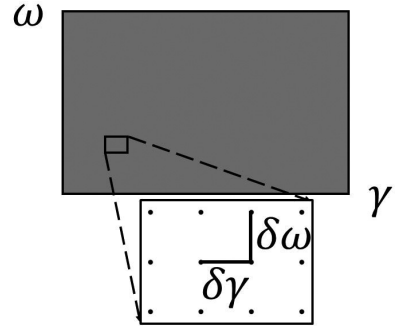


FIG. 16. Schematic diagram of the grid constructed in parameter space. In the calculations the values  $\delta\gamma = \delta\omega = 0.0002$  were employed.

Therefore, we have

$$\begin{aligned} e^{i\pi(\hat{J}_z+j)} |N; j, m'\rangle &= \frac{1}{\sqrt{N!}} \left( \hat{a}^{\dagger} + \frac{2\gamma}{\omega\sqrt{N}} m' \right)^N \Big|_{\alpha = -\frac{2\gamma m'}{\omega\sqrt{N}}} |j - m'\rangle. \end{aligned} \quad (\text{B3})$$

On the other hand, by using the properties of the coherent states, it is straightforward to show that  $e^{i\pi\hat{a}^{\dagger}\hat{a}} (\hat{a}^{\dagger})^k |\alpha\rangle = (-1)^k (\hat{a}^{\dagger})^k |-\alpha\rangle$ . With the previous result we obtain

$$\begin{aligned} e^{i\pi\hat{a}^{\dagger}\hat{a}} |N; j, m'\rangle &= (-1)^N \frac{1}{\sqrt{N!}} \left( \hat{a}^{\dagger} - \frac{2\gamma}{\omega\sqrt{N}} m' \right)^N \Big|_{\alpha = \frac{2\gamma m'}{\omega\sqrt{N}}} |jm'\rangle. \end{aligned} \quad (\text{B4})$$

By putting together Eqs. (B3) and (B4) we obtain  $\hat{\Pi} |N; j, m'\rangle = (-1)^N |N; j, -m'\rangle$ .

Then, the invariant subspaces of the parity operator are generated by states (46) with the same values  $N$  and  $|m'\rangle$ . It is straightforward to diagonalize the parity operator in these subspaces, and we obtain the eigenstates of the Dicke Hamiltonian in the limit  $\omega_0 \rightarrow 0$ , which are simultaneously eigenstates of the parity operator  $\hat{\Pi}$ ,

$$\begin{aligned} |N; j, m'; p = \pm\rangle &= \frac{1}{\sqrt{2(1 + \delta_{m',0})}} [|N; j, m'\rangle \pm (-1)^N |N; j, -m'\rangle]. \end{aligned} \quad (\text{B5})$$

Using this basis we can separate from the beginning the two parity sectors of the Dicke model and the extended coherent basis, which has been shown [49,51] to be very efficient to study large Dicke systems.

## APPENDIX C: NUMERICAL CALCULATIONS AND GRID IN PARAMETER SPACE

Numerical effort was indispensable in our shown results, in this way we construct rectangular grids in the parameter space according to the zone of study, this grids are composed for a significant number of points in which each point correspond to the calculation of  $\hat{H}$  with their eigenstates and energies, respectively, as was mentioned in Appendix B. In special to solve computationally the Dicke model with

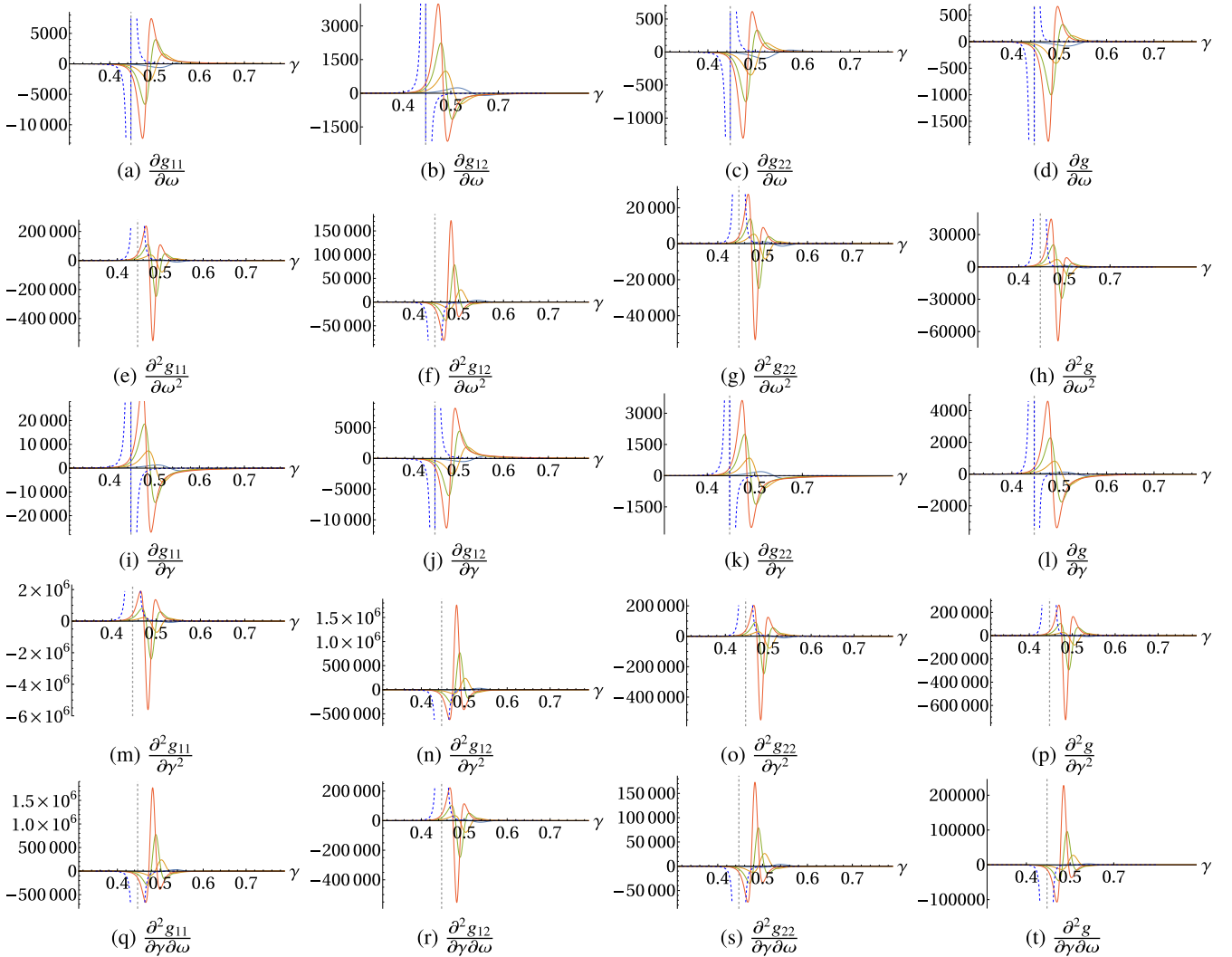


FIG. 17. Derivatives of the QMT components and its determinant in the thermodynamic limit (dashed blue) and in the case  $j = 5$  (solid blue),  $j = 10$  (solid orange),  $j = 15$  (solid green), and  $j = 20$  (solid red) with  $\omega_0 = 1$  and  $\omega = 0.8$ .

$j = 20$  and  $N_{\max} = 70$  we require approximately 200 MB of computer resources by point fixed in the parameter space. Once we have eigenstates, energies, and the respective operators defined in Eq. (5) we have all the tools to calculate numerically the elements of the QMT  $g_{ij}^{(0)}$  point by point. Subsequently, to obtain QMT elements numerically with a high resolution in the parameter space (see Fig. 16) we use the command `Interpolation[... , Method->Hermite]` defined in Mathematica to have  $g_{ij}$  as a continuous function, in this way we can use the analytical Eq. (6) and finally we obtain Ricci scalar  $R$ .

To give us one idea of the quantity of resources employed to obtain Figs. 8(b), 8(d), 8(f), 8(h), and

13, we have a parameter space domain defined in  $\gamma \in [0.01, 0.05]$  and  $\omega \in [0.16, 0.2]$  which implies 40 000 points that together are equivalent to 8 TB of computer resources. Fortunately, to do this calculations efficiently we employ around 50 parallelized institutional clusters (each cluster having Architecture: x86\_64, Processor: Intel(R) Xeon(R) Silver 4216 CPU @ 2.10GHz, CPUS: 32) and in few days we obtained our results.

#### APPENDIX D: DERIVATIVES OF THE QMT

All first and second derivatives of the QMT components and its determinant are shown in Fig. 17.

- [1] J. P. Provost and G. Vaille, *Commun. Math. Phys.* **76**, 289 (1980).  
 [2] P. Zanardi, P. Giorda, and M. Cozzini, *Phys. Rev. Lett.* **99**, 100603 (2007).

- [3] P. Kumar, S. Mahapatra, P. Phukon, and T. Sarkar, *Phys. Rev. E* **86**, 051117 (2012).  
 [4] S.-J. Gu, *Int. J. Mod. Phys. B* **24**, 4371 (2010).

- [5] A. Carollo, D. Valenti, and B. Spagnolo, *Phys. Rep.* **838**, 1 (2020).
- [6] A. T. Rezakhani, D. F. Abasto, D. A. Lidar, and P. Zanardi, *Phys. Rev. A* **82**, 012321 (2010).
- [7] A. Dey, S. Mahapatra, P. Roy, and T. Sarkar, *Phys. Rev. E* **86**, 031137 (2012).
- [8] D. Gonzalez, D. Gutiérrez-Ruiz, and J. D. Vergara, *Phys. Rev. E* **104**, 014113 (2021).
- [9] R. H. Dicke, *Phys. Rev.* **93**, 99 (1954).
- [10] K. Hepp and E. H. Lieb, *Ann. Phys. (NY)* **76**, 360 (1973).
- [11] K. Hepp and E. H. Lieb, *Phys. Rev. A* **8**, 2517 (1973).
- [12] Y. K. Wang and F. T. Hioe, *Phys. Rev. A* **7**, 831 (1973).
- [13] C. Emary and T. Brandes, *Phys. Rev. E* **67**, 066203 (2003).
- [14] B. M. Garraway, *Philos. Trans. R. Soc. London Sect. A* **369**, 1137 (2011).
- [15] P. Pérez-Fernández, P. Cejnar, J. M. Arias, J. Dukelsky, J. E. García-Ramos, and A. Relaño, *Phys. Rev. A* **83**, 033802 (2011).
- [16] A. Altland and F. Haake, *Phys. Rev. Lett.* **108**, 073601 (2012).
- [17] H. Shen, P. Zhang, R. Fan, and H. Zhai, *Phys. Rev. B* **96**, 054503 (2017).
- [18] S. Lerma-Hernández, J. Chávez-Carlos, M. A. Bastarrachea-Magnani, L. F. Santos, and J. G. Hirsch, *J. Phys. A* **51**, 475302 (2018).
- [19] S. Lerma-Hernández, D. Villaseñor, M. A. Bastarrachea-Magnani, E. J. Torres-Herrera, L. F. Santos, and J. G. Hirsch, *Phys. Rev. E* **100**, 012218 (2019).
- [20] M. Kloc, P. Stránský, and P. Cejnar, *Phys. Rev. A* **98**, 013836 (2018).
- [21] P. Kirton, M. M. Roses, J. Keeling, and E. G. Dalla Torre, *Adv. Quantum Technol.* **2**, 1800043 (2019).
- [22] D. De Bernardis, T. Jaako, and P. Rabl, *Phys. Rev. A* **97**, 043820 (2018).
- [23] A. Frisk Kockum, A. Miranowicz, S. De Liberato, S. Savasta, and F. Nori, *Nat. Rev. Phys.* **1**, 19 (2019).
- [24] P. Forn-Díaz, L. Lamata, E. Rico, J. Kono, and E. Solano, *Rev. Mod. Phys.* **91**, 025005 (2019).
- [25] A. Le Boité, *Adv. Quantum Technol.* **3**, 1900140 (2020).
- [26] C. Lewenkopf, M. Nemes, V. Marvulle, M. Pato, and W. Wreszinski, *Phys. Lett. A* **155**, 113 (1991).
- [27] C. Emary and T. Brandes, *Phys. Rev. Lett.* **90**, 044101 (2003).
- [28] M. A. Bastarrachea-Magnani, S. Lerma-Hernández, and J. G. Hirsch, *Phys. Rev. A* **89**, 032102 (2014).
- [29] M. A. Bastarrachea-Magnani, B. L. del Carpio, S. Lerma-Hernández, and J. G. Hirsch, *Phys. Scr.* **90**, 068015 (2015).
- [30] M. A. Bastarrachea-Magnani, B. López-del-Carpio, J. Chávez-Carlos, S. Lerma-Hernández, and J. G. Hirsch, *Phys. Rev. E* **93**, 022215 (2016).
- [31] J. Chávez-Carlos, M. A. Bastarrachea-Magnani, S. Lerma-Hernández, and J. G. Hirsch, *Phys. Rev. E* **94**, 022209 (2016).
- [32] J. Chávez-Carlos, B. López-del-Carpio, M. A. Bastarrachea-Magnani, P. Stránský, S. Lerma-Hernández, L. F. Santos, and J. G. Hirsch, *Phys. Rev. Lett.* **122**, 024101 (2019).
- [33] R. J. Lewis-Swan, A. Safavi-Naini, J. J. Bollinger, and A. M. Rey, *Nat. Commun.* **10**, 1581 (2019).
- [34] S. Pilatowsky-Cameo, J. Chávez-Carlos, M. A. Bastarrachea-Magnani, P. Stránský, S. Lerma-Hernández, L. F. Santos, and J. G. Hirsch, *Phys. Rev. E* **101**, 010202(R) (2020).
- [35] D. Villaseñor, S. Pilatowsky-Cameo, M. A. Bastarrachea-Magnani, S. Lerma-Hernández, L. F. Santos, and J. G. Hirsch, *New J. Phys.* **22**, 063036 (2020).
- [36] S. Pilatowsky-Cameo, D. Villaseñor, M. A. Bastarrachea-Magnani, S. Lerma-Hernández, L. F. Santos, and J. G. Hirsch, *Nat. Commun.* **12**, 852 (2021).
- [37] M. P. Baden, K. J. Arnold, A. L. Grimsmo, S. Parkins, and M. D. Barrett, *Phys. Rev. Lett.* **113**, 020408 (2014).
- [38] Z. Zhang, C. H. Lee, R. Kumar, K. J. Arnold, S. J. Masson, A. L. Grimsmo, A. S. Parkins, and M. D. Barrett, *Phys. Rev. A* **97**, 043858 (2018).
- [39] J. Cohn, A. Safavi-Naini, R. J. Lewis-Swan, J. G. Bohnet, M. Gärtner, K. A. Gilmore, J. E. Jordan, A. M. Rey, J. J. Bollinger, and J. K. Freericks, *New J. Phys.* **20**, 055013 (2018).
- [40] A. Safavi-Naini, R. J. Lewis-Swan, J. G. Bohnet, M. Gärtner, K. A. Gilmore, J. E. Jordan, J. Cohn, J. K. Freericks, A. M. Rey, and J. J. Bollinger, *Phys. Rev. Lett.* **121**, 040503 (2018).
- [41] T. Jaako, Z.-L. Xiang, J. J. Garcia-Ripoll, and P. Rabl, *Phys. Rev. A* **94**, 033850 (2016).
- [42] Y.-Q. Ma, S. Chen, H. Fan, and W.-M. Liu, *Phys. Rev. B* **81**, 245129 (2010).
- [43] M. V. Berry, *Proc. R. Soc. London Ser. A* **392**, 45 (1984).
- [44] M. Born and V. Fock, *Z. Phys.* **51**, 165 (1928).
- [45] O. Castaños, E. Nahmad-Achar, R. López-Peña, and J. G. Hirsch, *AIP Conf. Proc.* **1323**, 40 (2010).
- [46] T. Holstein and H. Primakoff, *Phys. Rev.* **58**, 1098 (1940).
- [47] D. Gonzalez, D. Gutiérrez-Ruiz, and J. D. Vergara, *J. Phys. A: Math. Theor.* **53**, 505305 (2020).
- [48] F. Wilczek and A. Zee, *Phys. Rev. Lett.* **52**, 2111 (1984).
- [49] M. A. Bastarrachea-Magnani and J. G. Hirsch, *Phys. Scr.* **2014**, 014005 (2014).
- [50] D. Gonzalez, D. Gutiérrez-Ruiz, and J. D. Vergara, *Phys. Rev. E* **99**, 032144 (2019).
- [51] J. G. Hirsch and M. A. Bastarrachea-Magnani, *Phys. Scr.* **2014**, 014018 (2014).
- [52] D. Gutiérrez-Ruiz, D. Gonzalez, J. Chávez-Carlos, J. G. Hirsch, and J. D. Vergara, *Phys. Rev. B* **103**, 174104 (2021).
- [53] M. A. Bastarrachea-Magnani, S. Lerma-Hernández, and J. G. Hirsch, *Phys. Rev. A* **89**, 032101 (2014).
- [54] M. Pandey, P. W. Claeys, D. K. Campbell, A. Polkovnikov, and D. Sels, *Phys. Rev. X* **10**, 041017 (2020).
- [55] M. A. Nielsen, M. R. Dowling, M. Gu, and A. C. Doherty, *Science* **311**, 1133 (2006).
- [56] N. Jaiswal, M. Gautam, and T. Sarkar, *Phys. Rev. E* **104**, 024127 (2021).
- [57] J. L. Gómez-Muñoz and F. Delgado, Quantum Mathematica Add-on, <http://homepage.cem.itesm.mx/lgomez/quantum/> (2011), accessed on Nov. 10, 2021.